Raman characterization of 0.4 nm single-walled carbon nanotubes formed in the channels of

AlPO$_4$-5 zeolite single crystals

Raman characterization of 0.4 nm single-walled carbon nanotubes formed in the channels of AlPO$_4$-5 zeolite single crystals

J T Ye, J P Zhai and Z K Tang[1]

Department of Physics and Institute of Nano-Science and Technology, Hong Kong University of Science and Technology, Clear Water Bay, Kowloon, Hong Kong, People's Republic of China

E-mail: phzktang@ust.hk

Abstract

In this paper, we review our recent research on ultra-small single-walled carbon nanotubes (SWNTs). Using Raman scattering as a tool, we systematically studied the pyrolysis process of carbon precursors in the channels of AlPO$_4$-5 zeolite single crystals, and studied the formation process of the ultra-small SWNTs in the channels. The thermal expansion behaviour and thermal stability of these ultra-small SWNTs, either confined in the AlPO$_4$-5 channels or in a freestanding environment, were also studied as a function of temperature. The *in situ* Raman-scattering measurement under 1×10^{-5} mbar showed that the (3, 3) and (4, 2) tubes were totally destroyed at a temperature of about 700 K, while the (5, 0) tube can survive to 790 K. The electronic states of the 0.4 nm SWNTs were modulated by means of lithium doping. The continuous electron charge transfer from lithium atoms to the tubes was traced using Raman scattering. With increasing doping level, the radial breathing modes of these tubes shifted to higher frequency because the vibration perpendicular to the tube axis was depressed, in contrast to the conventional softening and downshift of the tangential G-mode vibrations.

(Some figures in this article are in colour only in the electronic version)

1. Introduction

Using transition metals as catalysts, carbon nanotubes can be synthesized with only a single wall of graphene sheet [1, 2]. The diameter of each freestanding single-walled carbon nanotube (SWNT) ranges from 0.7 nm to a few tens of nanometres. SWNTs with diameters smaller than 0.7 nm are very unstable in free space, because of their extreme curvature and reactivity of

---

[1] Author to whom any correspondence should be addressed.

these structures [3, 4]. Small sized carbon nanotubes can be stabilized in a spatially confined environment. For example, the carbon nanotubes with diameters of only 0.5 nm [5] and 0.4 nm [6] are stable when they are confined in the centre of multi-walled carbon nanotubes. We have fabricated 0.4 nm SWNTs accommodated in 1 nm sized channels of $AlPO_4$-5 (IUPAC code AFI) single crystals [7–9]. These 0.4 nm SWNTs are mono-dispersed in size and perfectly aligned along the crystal channels, which brings experimental study for one-dimensional electronic systems closer to the theoretical model. When a carbon nanotube is not very small, its electronic structure can be predicted using a simple band-folding approximation. It is predicted that armchair tubes are metallic, while all other tubes are either small-gap semiconductors or insulators depending on the nanotube radius and chirality [10–12]. In very small SWNTs, however, the presence of σ^*–π^* hybridization introduced by the strong curvature effect leads to deviations of electronic properties from the prediction of band-folding theory. The influences of curvature effect on the electronic structures are observed in the optical absorption [13] and resonant Raman scattering [14–16]. Furthermore, the increased curvature enhances electron–phonon coupling, which makes carbon nanotubes superconducting [17], which was indeed observed in 0.4 nm SWNTs with a mean-field superconducting temperature of 15 K [18].

In this paper, we review Raman characterization of the 0.4 nm SWNTs. To improve structural quality of the 0.4 nm SWNTs, Raman scattering is used as a tool to monitor the pyrolysis processes of carbon precursors, and the formation process of carbon nanotubes in the AFI channels. The thermal properties of SWNTs@AFI as well as freestanding 0.4 nm SWNTs are also studied by investigating the temperature behaviour of Raman spectra measured at different temperatures. The lithium intercalated SWNTs@AFI system was characterized by Raman spectroscopy. It was found that there exists significant charge transfer from the lithium atoms to the SWNTs, leading to a modulated change in electron density near the Fermi energy level.

2. Experimental details

2.1. Synthesis of AFI crystals

Aluminophosphate AFI crystal is one of the few porous single crystals that can be synthesized in sub-millimetre size. The framework of the AFI crystal consists of alternating tetrahedrons of $(AlO_4)^-$ and $(PO_4)^+$, which form the hexagonal $P6cc$ structure with open channels along the (001) direction. The inner diameter of the channel is 0.73 nm, and the distance between two neighbouring parallel channels is 1.37 nm. AFI single crystals were grown by means of a hydrothermal process. As for many other zeolite crystals, as-grown AFI single crystals are usually rich in structural defects and their crystal sizes are usually limited to a few tens of micrometres. The growth of large-size AFI single crystals with high structural perfection is crucial in producing high-quality SWNTs in the crystal channels. We observed that addition of F^- ions to the starting gel is favourable to get large-sized single crystals and improve the optical grade of the crystals [19]. The function of the F^- ions is to restrain nucleation in the growth gel. In our experiment, 85% H_3PO_4 and aluminium isopropoxide were used as starting reactants. Tripropylamine $((CH_3CH_2CH_2)_3N$, hereafter named as TPA) molecules were used as the template for building up the AFI crystal framework. The TPA molecules also served as the carbon precursor for producing carbon nanotubes in the AFI channels. A pure AFI crystal is optically transparent from ultraviolet to near infrared wavelength regions, and is highly electrically insulating, which provides a perfect template framework for studying optical and electrical properties of nano-materials accommodated in the channels.

2.2. Synthesis of single-walled carbon nanotubes

SWNTs were produced by pyrolysing the TPA carbon precursors in the AFI channels [7–9]. When the TPA containing crystals were treated at a temperature of $600\,°C$ for several hours, the crystals changed colour from transparent to dark brown with high absorption for the light polarized parallel to the *c*-axis of the crystal, and transparent for the light polarized perpendicular to the *c*-axis. High-resolution transmission electron microscope (HRTEM) [8, 20, 21] and x-ray diffraction [22] experiments all confirmed that the nanotubes produced in the AFI channels are of a diameter as small as 0.4 nm.

2.3. Raman characterization

Raman spectra of the 0.4 nm SWNTs were measured using a Jobin Yvon T64000 triple-grating micro-Raman system equipped with a CCD detector cooled by liquid nitrogen. 14 laser lines with different wavelengths of an Ar–Kr laser were used to excite the samples. The laser line at 355 nm from a third harmonic of a YVO laser was used as the excitation in the UV region. The excitation laser light was focused onto the samples using a $40\times$ or $100\times$ objective. For all the spectra, the laser excitation powers were limited to a level below 1 mW.
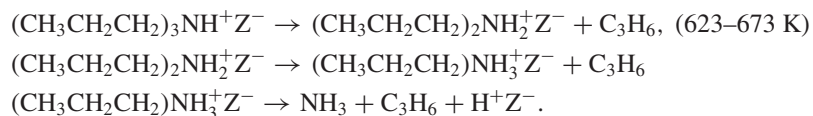
3. Results and discussions

3.1. Effect of F^- ions on the pyrolysis of TPA carbon precursors in the AFI channels

As mentioned above, proper addition of F^- ions to the starting gel of AFI synthesis is favourable to increase the size and improve the quality of AFI single crystals. The existence of F^- ions, however, seems not to be favourable to the pyrolysis of the TPA carbon precursor [23]. The TPA molecules in the AFI channels exist in the form of $(CH_3CH_2CH_2)_3NH^+OH^-$ in the AFI framework without F^- ions, and $(CH_3CH_2CH_2)_3NH^+F^-$ in the AFI framework with F^- ions. In comparison with the binding between $(CH_3CH_2CH_2)_3NH^+$ and OH^- ions, the binding force between $(CH_3CH_2CH_2)_3NH^+$ and F^- ions is significantly stronger, implying that it is more difficult to decompose the carbon precursor of $(CH_3CH_2CH_2)_3NH^+F^-$ than $(CH_3CH_2CH_2)_3NH^+OH^-$. Thermogravimetry and mass spectral analysis showed that a significant amount of the carbon precursors $(CH_3CH_2CH_2)_3NH^+F^-$ was lost (escaped from the crystal channels) at the pyrolysis temperature [23], leading to insufficient remaining carbon atoms in the channels to form continuous carbon nanotubes.

3.2. Catalyst effect of Si^{4+} ions on the pyrolysis of carbon precursors

Detailed investigation showed that even without existence of F^- ions in the framework of AFI, the loss of carbon precursors during pyrolysis is still not negligible. The reason is that the channel walls of pure AFI crystals are relatively inert, and the adsorption force between the walls and the precursor molecules is weak. We adopted two approaches to improve the filling density of the nanotubes in the channels and structural quality of nanotubes as well: (1) to enhance the adsorption force of the channel walls by means of introducing localized electric dipoles onto the walls, and (2) to decrease the pyrolysis temperature of the carbon precursors in the channels by means of generating catalytic Brønsted acid sites on the channel walls. These approaches were realized by replacing some P^{5+} elements in the framework using Si^{4+} [23, 24]. Around the lattice sides of Si^{4+}, the channel walls were negatively charged (Z^-), and thus have a strong force to attract carbon precursor ions in the form of $(CH_3CH_2CH_2)_3NH^+Z^-$. The cations of the carbon precursors are strongly attracted by the negative charged lattice. The

subsequent pyrolysis reaction of the $(CH_3CH_2CH_2)_3NH^+Z^-$ can be described as follows:

$$(CH_3CH_2CH_2)_3NH^+Z^- \rightarrow (CH_3CH_2CH_2)_2NH_2^+Z^- + C_3H_6, \ (623–673 \ K)$$
$$(CH_3CH_2CH_2)_2NH_2^+Z^- \rightarrow (CH_3CH_2CH_2)NH_3^+Z^- + C_3H_6$$
$$(CH_3CH_2CH_2)NH_3^+Z^- \rightarrow NH_3 + C_3H_6 + H^+Z^-.$$

Decomposition of the $(CH_3CH_2CH_2)_3NH^+Z^-$ composites leads to a successive release of C_3H_6 molecules. These C_3H_6 molecules can be either pyrolysed into smaller molecules (such as CH_4 and C_2H_4) and subsequently carbonized in the channels, or converted into bigger molecules such as 2-methylbutane and xylene. These carbonization or conversion processes are evidenced by characteristic signals of C_2H_4 in mass spectra [23, 24]. The number of carbon atoms kept inside the channels is determined by the competition between the carbonization and conversion processes. All signals became weaker and finally undetectable when the sample was heated up to 823 K, indicating a complete carbonization of the carbon precursors. In comparison with pure AFI single crystals, the decomposition temperature of the carbon precursors inside the channels of Si-decorated AFI crystals is also notably decreased, owing to the catalytic effect of Brønsted acid sites.

3.3. Raman characterization of SWNTs generated in the metal-ion decorated channels

Besides silicon substitution as discussed above, we systematically studied the catalyst effect of various metal cations on the decomposition of the carbon precursors. Figure 1(a) shows the Raman spectra of the SWNTs fabricated in the channels of MeAPO-5 (Me = Ti, V, Mn, Mg, Co, and Si) single crystals excited by the 514.5 nm line of an Ar–Kr laser. Generally, the Raman spectra of the 0.4 nm SWNTs exhibit three main features: the radial-breathing modes (RBMs) in the low-frequency region (400–600 cm^{-1}), the D bands due to disordered carbon structures in the intermediate-frequency region (1200–1500 cm^{-1}) and the tangential graphite-like G bands in the high-frequency region (1500–1620 cm^{-1}). The signals at 510 and 550 cm^{-1} are attributed to RBMs of the chiral (4, 2) nanotubes and the zigzag (5, 0) nanotubes, respectively [25]. The RBM signal at 580 cm^{-1} due to the (3, 3) armchair tube is highly sample dependent. It can be clearly seen in some crystals; however, in most of samples, this RBM signal only shows as a small shoulder. The reason for the weak Raman feature is possibly due to an improper resonant condition, since the optical transition energy of the (3, 3) tube is around 3.0 eV [13], which is much higher than the energy of the excitation laser line. As the RBM signals are the fingerprint of nanotube structures, the Raman intensity ratio of the RBM signals I_{RBM} to the G-like Raman signal I_{RBM}/I_G is a good indicator of the filling density of carbon nanotubes in the AFI channels. The relative integrated RBM intensity is plotted by the solid square in figure 1(b) for the SWNTs generated in the channels of MeAPO-5 with different metal cations. The relative intensities of the RBM signals for the SWNTs in MgAPO-5, MnAPO-5, CoAPO-5, and SAPO-5 crystals are significantly higher than those in pure AFI crystals, indicating better quality and higher filling density of SWNTs in the channels of these decorated crystals. The effect of Ti and V cations, however, seems marginal, as no significant improvement in RBM intensity is seen in these samples. Among these crystals, the intensity of the disorder-related D band near 1430 cm^{-1} in MgAPO-5, MnAPO-5, CoAPO-5, and SAPO-5 crystals is relatively low, indicating the better structural quality of the SWNTs in these crystals. These experimental results agree well with the predictions of first-principles calculations, which showed that the metal-incorporated frameworks were more favourable for the SWNT formation [26].
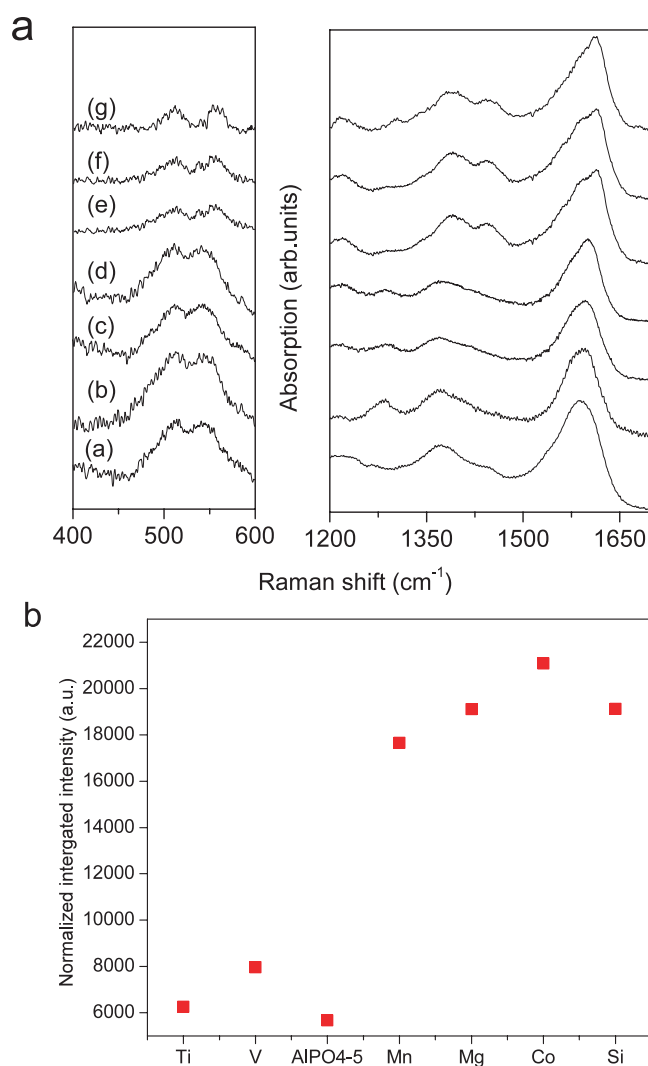
Figure 1. Raman spectra of the SWNTs fabricated in the channels of MeAPO-5 single crystals: (a) SWNT@SAPO-5, (b) SWNT@CoAPO-5, (c) SWNT@MgAPO-5, (d) SWNT@MnAPO-5, (e) SWNT@AlPO$_4$-5, (f) SWNT@TiAPO-5, and (g) SWNT@VAPO-5. The lower panel shows the integrated relative intensity of the RBMs.

3.4. Raman spectra of the SWNTs generated using different carbon precursors

The number of carbon atoms per precursor molecule is another crucial factor affecting the formation of SWNTs. We have used several different carbon precursors; they are (CH$_3$CH$_2$)$_3$N (TEA), (CH$_2$OHCH$_2$)$_3$N (TEOA), (CH$_3$CH$_2$CH$_2$)$_3$N (TPA), (CH$_3$CH$_2$CH$_2$)$_4$NOH (TPAOH), and (CH$_3$CH$_2$CH$_2$CH$_2$)$_4$NOH (TBAOH), respectively. The Raman spectra of the SWNTs produced using these carbon precursors are shown in figure 2. Again, we use the Raman intensity ratio of the RBM to the G band (I_{RBM}/I_G) as a measure of the tubular carbon structure contained in the AFI channels. The relative intensities of the RBM bands at 510 and 550 cm^{-1} are obviously enhanced with increase in the carbon number per precursor molecule, while the
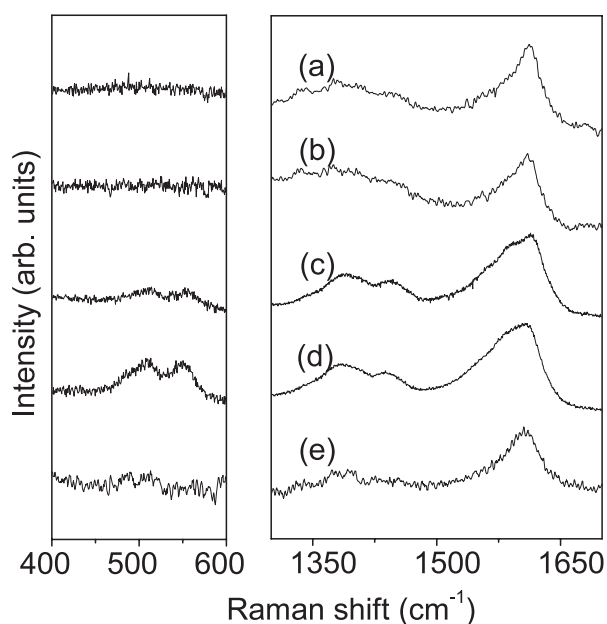
Figure 2. Raman spectra of the SWNT@AlPO$_4$-5 crystal using the 514.5 nm laser line, produced by pyrolysing various carbon precursors in the channels: (a) TEA, (b) TEOA, (c) TPA, (d) TPAOH, and (e) TBAOH.

line width of the G band near 1600 cm^{-1} became small upon the increase of carbon atoms per molecule from 6 to 12 (from TEA and TEAOH to TPAOH), indicating better structural quality and higher occupation rate of nanotubes in the channels. For the TBAOH precursor, the number of carbon atoms per molecule is 16, the largest one among these precursor molecules. However, the relative intensity of the RBM signal is not as high as that of TPA precursors. The reason is that the TBAOH molecule is so big that it in fact occupies a channel space of more than one unit cell, so that the volume density of carbon in TBAOH adopted AFI crystals is not as high as that in TPA adopted crystals. We thus concluded that TPAOH is the most suitable carbon precursor for generating carbon nanotubes in the channels.

3.5. Raman spectra of the SWNTs under UV laser excitation

The as-grown SWNTs in pristine AFI crystals show a strong luminescence in the visible wavelength region [27]. The luminescence is especially strong for the samples in which the carbon precursor molecules are not completely carbonized. When the photon energy of the excitation laser light increases, the luminescence band shifts slightly towards shorter wavelength, as shown in figure 3(a). The peak wavelength of the luminescence is centred at 538 nm under the excitation of the 457.9 nm laser line. When excited using visible laser light, some important features of Raman signals are embedded into the strong luminescent background, which makes the real Raman signal difficult to detect. To avoid the influence of the strong luminescence background, we measured Raman spectra using UV laser excitation at 355 nm for the SWNTs. The general feature of the first-order UV Raman scattering is similar to that excited using visible laser lines: the D and G bands are clearly observed at 1400 and 1618 cm^{-1}. The overtones of the D and G modes are observed at 2800 and 3236 cm^{-1}, respectively. Between the overtones of D and G bands, there exists a clear Raman signal located
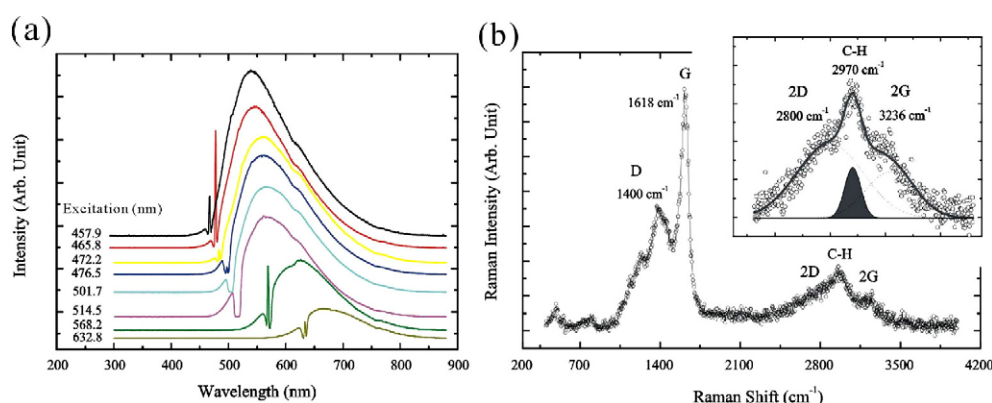
Figure 3. (a) Luminescence spectra of the SWNT@AFI crystals excited using laser lines ranging from 457.9 to 632.8 nm. (b) Raman spectra of a luminescent sample excited using the 355 nm laser line. The D and G bands are observed at 1400 and 1618 cm^{-1}, respectively. The inset shows the 2D and 2G overtones at 2800 and 3236 cm^{-1}. The carbon–hydrogen vibration is observed at 2970 cm^{-1}.

at 2970 cm^{-1}. This Raman line is attributed to the vibration of carbon–hydrogen bonding. Detailed investigation showed that there exists a close correlation between this C–H vibration signal and the intensity of luminescence of the sample. High-intensity luminescence of the sample is always accompanied by uncompleted dissociation of the C–H bonding of the carbon precursors.

3.6. Thermal properties of the SWNT@AFI crystals

The thermal properties of carbon nanotubes are of fundamental interest in both science and engineering [28, 29]. Extremely high thermal conduction coefficient along the tubule direction and anisotropic heat transfer properties due to their large aspect ratio are a few examples of the novel thermal properties of carbon nanotubes [12]. Applications of carbon nanotubes in a high-temperature environment require deeper understanding of the normal modes of vibration. Raman scattering measurement can characterize the properties of 'soft modes', which are directly related to the structural transition that determines the limits of engineering applications.

The temperature dependence of Raman spectra is closely related to the force between the carbon–carbon bonds, which is influenced by defects, disorder, and van der Waals interactions between nanotubes and accommodation channel walls. Figure 4(a) shows the temperature dependence of the RBMs in the temperature range from 80 to 870 K. The RBMs from the (4, 2) and the (5, 0) tubes at 510 and 550 cm^{-1} are resolved at all temperatures and show an evident upshift only at a temperature lower than 420 K. The RBM of the (3, 3) tube at 580 cm^{-1} only gives a very small contribution to the Raman spectra and cannot be clearly resolved.

For the nanotube–zeolite composite sample, the thermal properties might not be purely from SWNTs, the contribution from the host crystal framework is not ignorable. In figure 4(b), we schematically show the influence on the thermal expansion coefficient of the nanotubes from the zeolite frameworks. A molecular dynamic simulation shows that the thermal expansion coefficients for the (5, 5) and the (10, 10) tubes are 0.35×10^{-5} and 0.08×10^{-5} K^{-1} in the radial direction and 0.39×10^{-5} and 0.24×10^{-5} K^{-1} in the axial direction, respectively [30]. The thermal expansion coefficient of the AFI crystal is 1×10^{-5} K^{-1} [31], two to three times larger than the maximum expansion coefficient of the nanotubes. Hence, the confinement
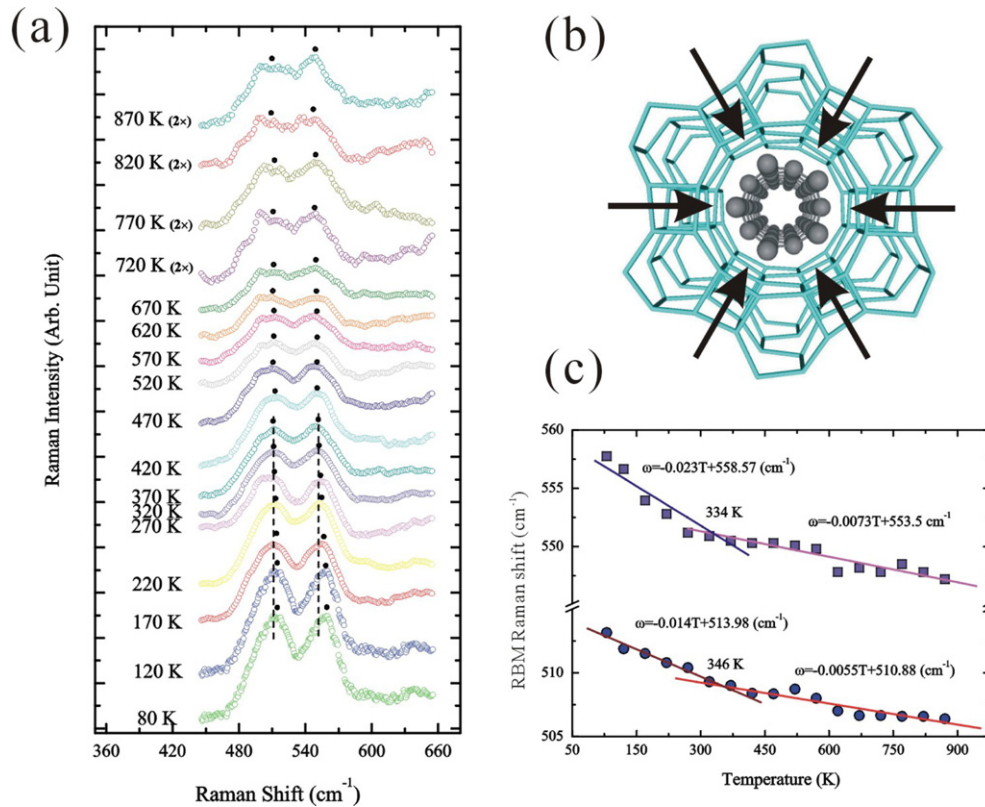
Figure 4. (a) Temperature dependence of the RBM Raman modes excited using the 632.8 nm laser line in the temperature range of 80–870 K. Two dashed lines mark the RBM frequency for the (4, 2) and the (5, 0) tubes, respectively. The positions of the RBMs at different temperatures are marked with dots. (b) Schematic presentation of the confinement of the SWNTs by the AFI framework channel at or below the temperature that the diameters of the AFI and the nanotubes match. (c) Frequency shift of the RBM modes which can be linearly fitted in two different temperature ranges of 80–370 and 420–870 K.

effect on the nanotube's thermal expansion cannot be ignored at or below a critical temperature at which the diameter of the channel is comfortable to accommodate the 0.4 nm nanotubes. However, at a temperature higher than the critical temperature, the SWNTs can vibrate more freely with a similar temperature dependence of vibration frequency as a typical freestanding SWNT. The vibration frequencies of the RBMs are plotted as a function of temperature in figure 4(c). As clearly seen in the figure, the thermal expansion coefficient (the curve slop) is different in the low and high temperature regions, with a turning temperature at around 340 K. For the (5, 0) tube, the vibration frequency is given by $\omega_{RBM} = -0.027\,T + 559.4$ cm^{-1} in the low-temperature region (80–370 K), and $\omega_{RBM} = -0.0071\,T + 553.39$ cm^{-1} in the high-temperature region (370–870 K). For the (4, 2) tube, the RBM frequency is given by $\omega_{RBM} = -0.014\,T + 513.87$ cm^{-1} and $\omega_{RBM} = -0.0062\,T + 511.44$ cm^{-1} in the low- and high-temperature regions, respectively. At high temperature, the mechanical interaction between the SWNTs and zeolite channel is small because the nanotube has more space to vibrate. Thus the thermal expansion coefficient of the nanotube at high temperature is very close to that of freestanding nanotubes [32]. In contrast, in the low-temperature range, the thermal expansion
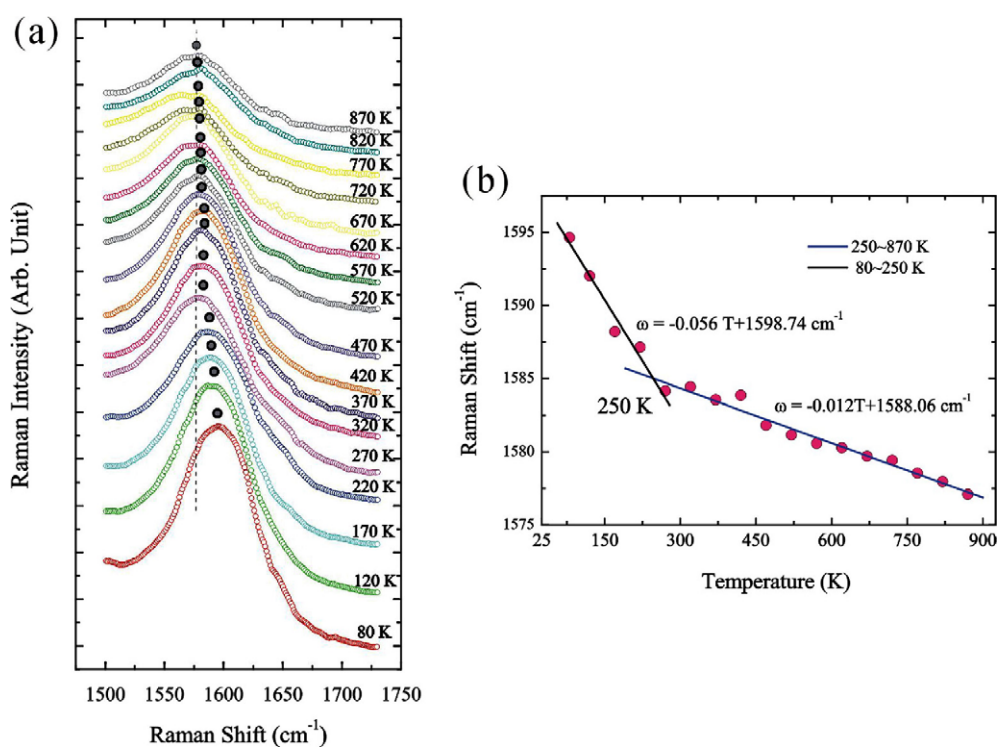
Figure 5. (a) Raman spectra excited by the G-band vibrations measured for the SWNT@AFI crystals using the 632.8 nm laser line in the temperature range of 80–870 K. (b) Raman shift of the G band plotted as a function of temperature.

coefficient is significantly larger than that of the freestanding nanotubes, making the vibration shift to higher frequency. This abnormal temperature behaviour is a direct reflection of the confinement effect of the zeolite framework. A similar effect has also been observed in a double-walled nanotube system [32]. The temperature dependence of the Raman spectra of the G band is shown in figure 5(a). In figure 5(b), we plotted the frequency of the G band against temperature. Again, we see two different characteristic slopes in the low- and high-temperature regions. These two slopes intersect at 250 K, which is about 100 K lower than that of the RBMs' vibration. As the G-band vibration corresponds to atomic displacement along the tangential directions of a cylindrical carbon surface, less influence from the AFI framework on the SWNTs is expected unless the space between the tube and the frameworks is sufficiently tight.

3.7. Thermal stability of the freestanding 0.4 nm SWNTs

Formation of nanotube structures can be viewed as a distortion of an atomic two-dimensional covalent bond in a graphene sheet. In small-diameter nanotubes, the energy cost of the distortion becomes severe as the angle of the carbon bond deviates more strongly from the $120°$ bond angle of the sp^2 hybridization in the graphene structure. Theoretical calculations showed that 0.4 nm is at or close to the lower limit of the diameter for a stable SWNT. A 0.4 nm SWNT is thermodynamically unstable [33], though energetically it is more favourable than its corresponding graphitic ribbon [34].
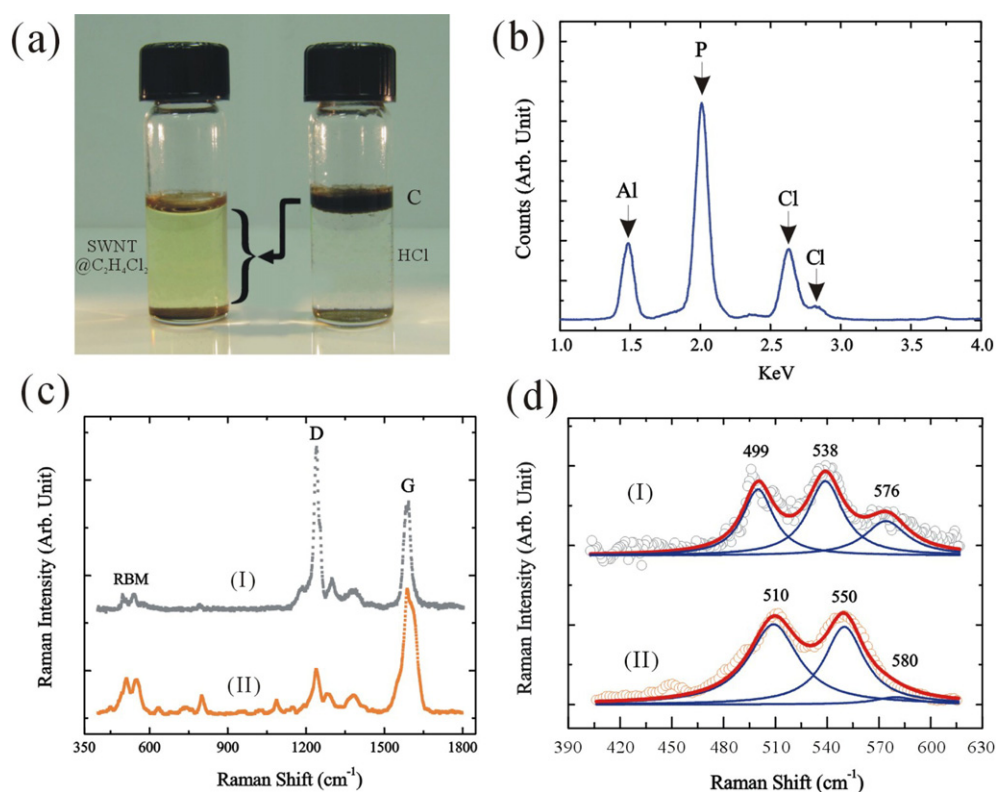
Figure 6. (a) Right bottle, dissolved SWNT@AFI zeolite in hydrochloride acid solution. Left bottle, the black layer of the right bottle was dispersed into dichloroethane solution. (b) XRF spectrum of the dried transparent layers from the right bottle, showing only elements of P and Al and Cl. (c) Raman spectra of the freestanding SWNTs (I) and SWNTs confined inside AFI crystals (II) at 300 K, excited using the 632.8 nm laser line. (d) Raman spectra of the RBMs of the freestanding SWNTs (I) and the confined SWNTs (II). The RBMs are fitted by three Lorentzian peaks for three possible tube structures.

Since the 0.4 nm SWNTs are originally formed inside the channels of AFI zeolites, to study the thermal properties of freestanding 0.4 nm SWNTs, the zeolite framework was dissolved by using hydrochloride acid. Figure 6(a) shows the chemical process of dissolving the AFI crystal and dispersing SWNTs into dichloroethane solvent. The AFI zeolite crystals are dissolved in hydrochloride (figure 6(a), the bottle on the right). The mixture was then separated into a black layer containing the carbon species and a transparent layer containing the dissolved frameworks. The black layer was then dispersed into dichloroethane to form the nanotube solution (the bottle on the left) and the transparent layer was dried and analysed by XRF. The XRF spectrum (figure 6(b)) showed that the transparent layer contains Al, P, and Cl, indicating separation of the zeolite framework and carbon species in the dissolving process. The Raman spectrum of the freestanding SWNTs, as shown in figure 6(c), is generally similar to that of the SWNTs@AFI. Nearly every spectral feature of the SWNTs is preserved in the spectra of the freestanding tubes. As a prominent distinction, however, the intensity of the disorder-related D bands is significantly enhanced, implying increased density of defects and disorders because of the marginal stability of the freestanding tubes. When the tubes are confined inside the restricted channels, the spread of defects formed during the fabrication process is effectively

depressed. When the tubes are released into free space, however, these defects are expected to grow vigorously.

It is noted that, in comparison with the confined SWNTs in the AFI channels, the linewidth of the RBMs is narrowed in the freestanding tubes, indicating a reduced interaction of SWNTs with channel walls. In figure 6(d), the Raman spectra in the RBM frequency region are magnified both for the freestanding and SWNTs@AFI. The three RBMs of the SWNTs@AFI crystal, located at 510, 550 and 580 cm^{-1} for the (4, 2), (5, 0) and (3, 3) tubes, were shifted to lower frequency in the freestanding tubes by 12 cm^{-1} for the (5, 0) tube, 11 cm^{-1} for the (4, 2) tube and 4 cm^{-1} for the (3, 3) tube, respectively. According to an *ab initio* first-principles calculation, the energy-relaxed diameter is 0.408 nm for the bare (5, 0) nanotube and 0.406 nm for the (5, 0) tube accommodated in the AFI channels [35]. The redshift of the RBMs can thus be attributed to a slight expansion of the SWNTs in diameter when they are released from the channel to the free space. The shifting of the Raman mode can also be due to the effect of the environment on the vibrational force constant. For example, the RBM is upshifted for SWNTs in a bundle in comparison with that of a freestanding tube since its radio vibration is affected by the interaction between individual tubes, while the diameter is not affected [36].

The stability of the freestanding 0.4 nm SWNTs at different temperature was monitored by means of Raman scattering. The Raman spectra measured in a vacuum of 10^{-5} Torr at different temperatures are shown in figure 7(a). With increasing temperature, the frequencies of the G band at 1589 cm^{-1} and the D band at 1239 cm^{-1} show collective downshifts. The temperature coefficient of the shift for the G band is -0.0246 cm^{-1} K^{-1}, which is comparable to the SWNTs with larger diameters of 1.3–1.4 nm [37]. The temperature coefficient of the Raman shift for the D bands is -0.0235 cm^{-1} K^{-1}, which is larger than that of large-sized tubes [30, 38]. It is noticed that the shift of the D band is comparable to that of the G band in the ultra-small SWNTs. Due to the large frequency splitting of the G-mode vibration along the tube direction (G$^+$ mode) and along the circumferential direction (G$^-$ mode) [39, 40], the G$^-$ band in these ultra-small carbon nanotubes overlaps with the D band. The large downshift in the D-band frequency might be determined by a combination of the temperature coefficient of the D and the G$^-$ bands.

Isothermal Raman spectra of the freestanding 0.4 nm SWNTs were measured by maintaining the temperature at 870 K for different heating times, as shown in figure 7(b). The Raman signals became weaker and broader upon the increase of heating duration. After isothermal heating for 30 min, the SWNTs were completely damaged and changed into amorphous carbon characterized by the broad Raman bands centred at 1300 and 1580 cm^{-1}. The spectrum shown at the bottom was measured when the temperature was cooled back to room temperature from 870 K. The spectrum maintains the amorphous-like feature and no nanotube modes are observable, indicating that the nanotube structure was permanently destroyed by heating at 870 K.

The thermal stability of the freestanding 0.4 nm SWNTs is much weaker than that of large-size SWNTs, which are reported to be thermally stable up to the graphite instability temperature around 4000 K [41]. The thermal damage temperature observed for the 0.4 nm SWNTs is even lower than that of 0.33 nm SWNTs predicted based on a tight-binding molecular dynamics simulation [42]. The results indicate that, for the SWNTs with such small diameters, the strong curvature effect significantly affects the stability of the SWNTs. The defects existing in the dissolved SWNTs might also play a significant role in lowering the thermal stability temperature.

More details on the structural transformation process were also investigated by analysis of the temperature dependence of the RBMs. As shown in figure 8, RBMs for SWNTs@AFI and freestanding SWNTs are compared side by side. Raman spectra in similar temperature ranges
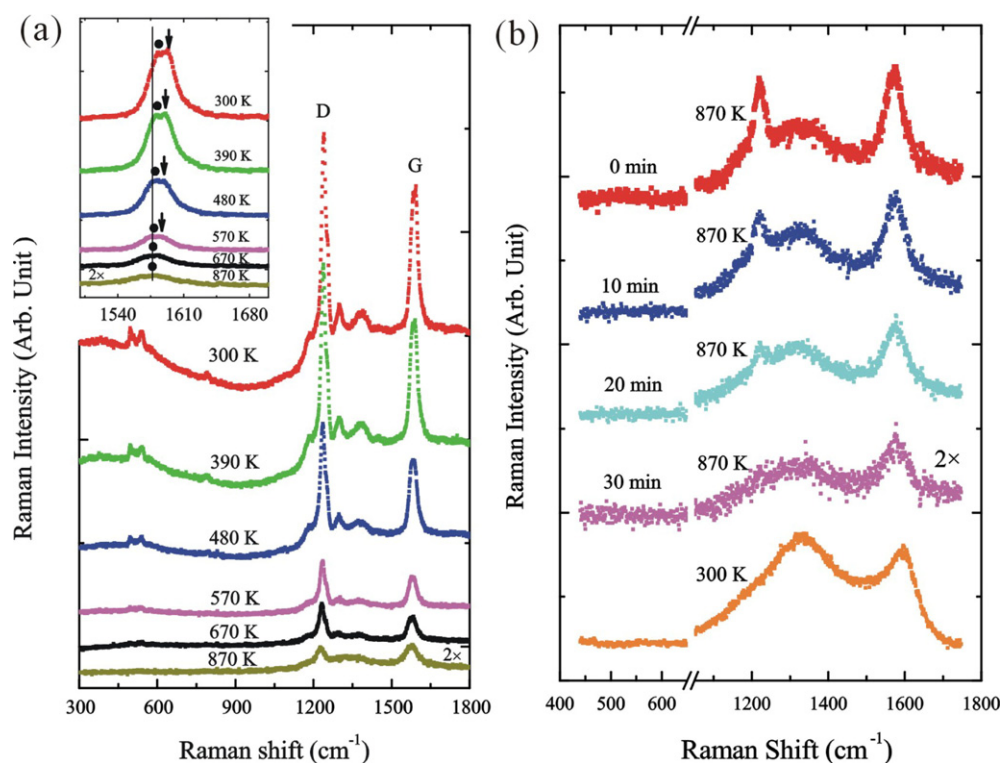
Figure 7. (a) Raman spectra of the freestanding SWNTs excited using the 632.8 nm laser line measured in the temperature region of 300–870 K. The inset shows the enlarged G band at different temperatures. The dots and arrows indicate the peak positions of two components in the asymmetric G bands showing a downshift and broadening with elevating temperature. The two components merge into a single symmetric peak at temperatures higher than 670 K. (b) Spectral changes under isothermal conditions at 870 K for different heating durations. The spectrum shown at the bottom is measured at 300 K cooling backed from the isothermal heating at 870 K.

are marked with the same colour in the left and right panels. Raman spectra of the confined sample indicate that all three carbon nanotube species are stable inside the zeolite framework even at 870 K, which strongly suggests that the confinement effect of the zeolite framework protects the SWNTs from breaking down even under high temperatures.

In the freestanding SWNTs, the intensity of the RBM Raman signals is decreased significantly and the line-width is broadened with increase of temperature. The decrease of the Raman intensity is related to the decrease of the SWNT population during the heating since the probability of phase transformation increases with time and temperature. All three structures survived up to 670 K, characterized by the three distinctive RBMs' Raman signals. An abrupt spectral change is observed at 730 K, at which the RBMs at 499 and 576 cm^{-1} are suddenly blurred. The main feature of the spectra then transforms from three distinctive peaks to a broad band centred at 538 cm^{-1}. This Raman band survived till to 790 K. The spectra measured above 800 K are weak and featureless. These results suggest that, among the three types of the 0.4 nm SWNTs, the (5, 0) tube with the zigzag structure is more stable than the other two structures. The structures of the (4, 2) and (3, 3) tubes are damaged at around 730 K, while the (5, 0) tube is stable up to 790 K. However, all three structures collapse at temperatures higher than 800 K.
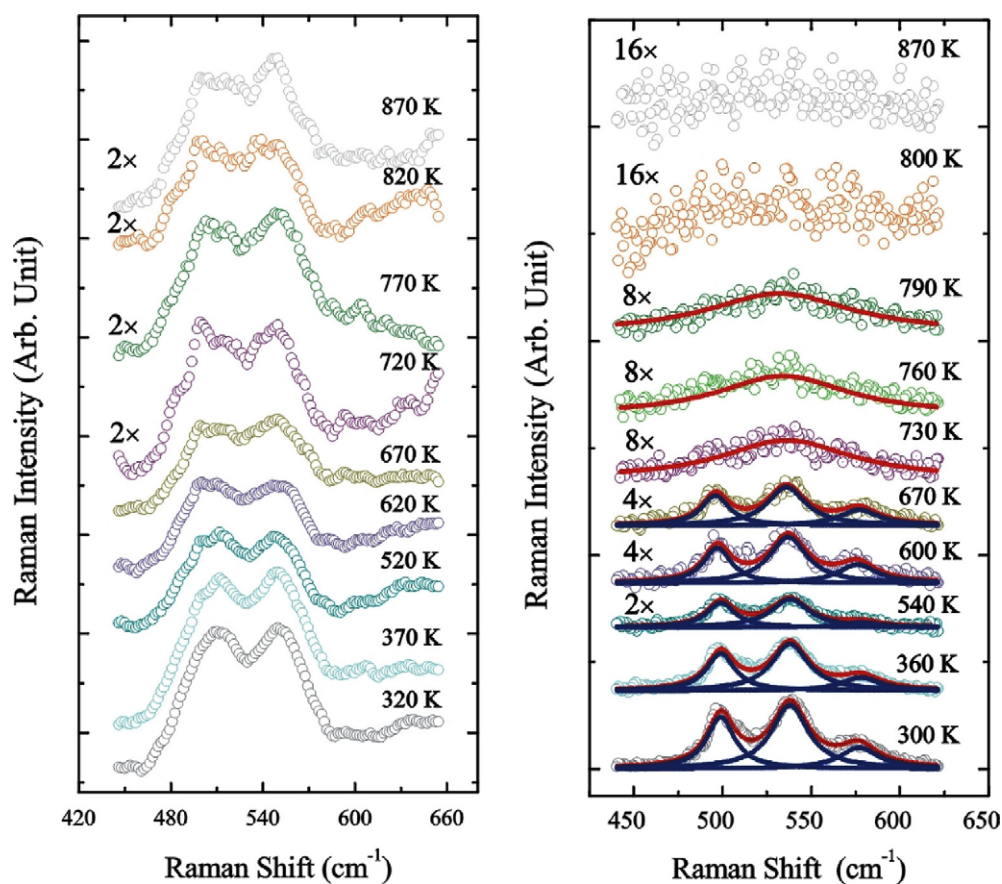
Figure 8. Raman spectra of the SWNTs@AFI crystals (left panel) and the freestanding SWNTs (right panel) excited using the 632.8 nm laser line at temperatures ranging from 300 to 870 K. The Raman spectra in the right panel are fitted using three Lorentzian line-shapes for three RBMs at or below 670 K. The spectra at temperature above 670 K can only be fitted with one Lorentzian component.

3.8. Raman characterization of lithium-doped SWNTs@AFI

The electronic states of carbon nanotubes can be modulated by doping of electron donors or acceptors [43]. By adding or depleting electrons from the Fermi surface, the Fermi level of the nanotubes can be raised or lowered to coincide with Van Hove singularities, leading to novel phenomena in optical and electrical properties [43, 44]. In comparison with many attempts at alkali atom intercalations in graphite and fullerenes, doping lithium into nanotubes is more attractive because carbon nanotubes are expected to be a new efficient anode material for rechargeable lithium-ion batteries. The alkali metal storage capacity of SWNT bundles is higher than that of graphite and disordered carbon. Shimoda *et al* showed that the reversible lithium storage capacity could increase from LiC_6 to LiC_3 when SWNTs are chemically etched to short segments [45].

A first-principles calculation has shown that there are several possible sites for lithium intercalation [46]. In addition to the interior of the tube, the lithium atoms may decorate the interstitial space between the outer wall of the tube and the inner wall of the AFI channels.
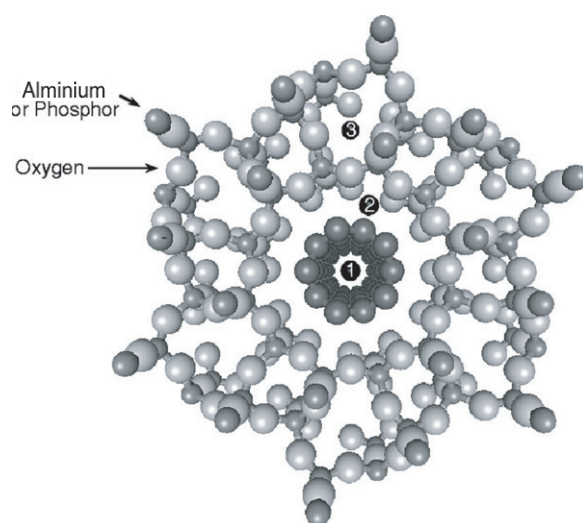
Figure 9. Ball-and-stick model of the AFI single crystal containing a zigzag (5, 0) tube. There are three possible locations for insertion of lithium indicated by numbered positions.

It is also possible to put them into the hexagonal interstices of the AFI frameworks. All these intercalating sites are marked in figure 9 on a ball-and-stick model of the SWNTs@AFI crystal. Calculation showed that the intercalation of lithium in the hexagonal interstices of AFI frameworks has the smallest possibility.

Lithium was doped into the SWNTs@AFI system by means of vapour phase adsorption. SWNTs@AFI crystals were sealed together with pre-distilled lithium metal into a Pyrex glass tube under 10^{-6} mbar and then heated at $220\,^{\circ}$C for 5 h. Then the crystal was sealed into a rectangular Pyrex tube with a 2×5 mm^2 cross section for optical measurements. Raman spectra were measured at room temperature using excitation of the 632.8 nm line of a He–Ne laser. In a sample with unsaturated doping level, the lithium concentration was high at the edges and gradually decreased from the edge to the centre of the zeolite crystal. By measuring spectra at different points from the edge to the centre, Raman scattering of the SWNTs with different densities of lithium doping was obtained. Figures 10 and 11 show the Raman spectra for different levels of lithium intercalation in the RBM (figure 10) and G-band (figure 11) frequency regions, respectively. Spectrum 0 is for the pristine crystal without lithium doping. The lithium concentration gradually increases from spectrum 0 to 10. With increase of the doping level, the intensities of the RBM signals for both the (4, 2) and (3, 3) tubes are decreased. The RBM of the (4, 2) tube even disappears in the saturated doping stage (spectrum 10). The RBM of the (5, 0) tube shifts slightly to a higher frequency with the doping, which can be understood in terms of enhanced stiffness of the SWNTs after insertion of lithium atoms. At the highest doping level (spectrum 10), the upward shift of the RBM of the (5, 0) tube is measured as 18 cm^{-1}, which is significantly smaller than the shift (74 cm^{-1}) observed in Br$_2$ doped SWNTs [43].

Based on polarization studies of Raman scattering on SWNT bundles [47] and theoretical predictions [12], the tangential G mode for a general chiral tube consists of three symmetries, A, E$_1$, and E$_2$, each of them further split into two lines denoted by G$^+$ and G$^-$ because of the curvature effect [48, 49]. The upper frequency, G^+, located near 1600 cm^{-1}, is associated with carbon atom displacement along the tube axis, which shows very small dependence on
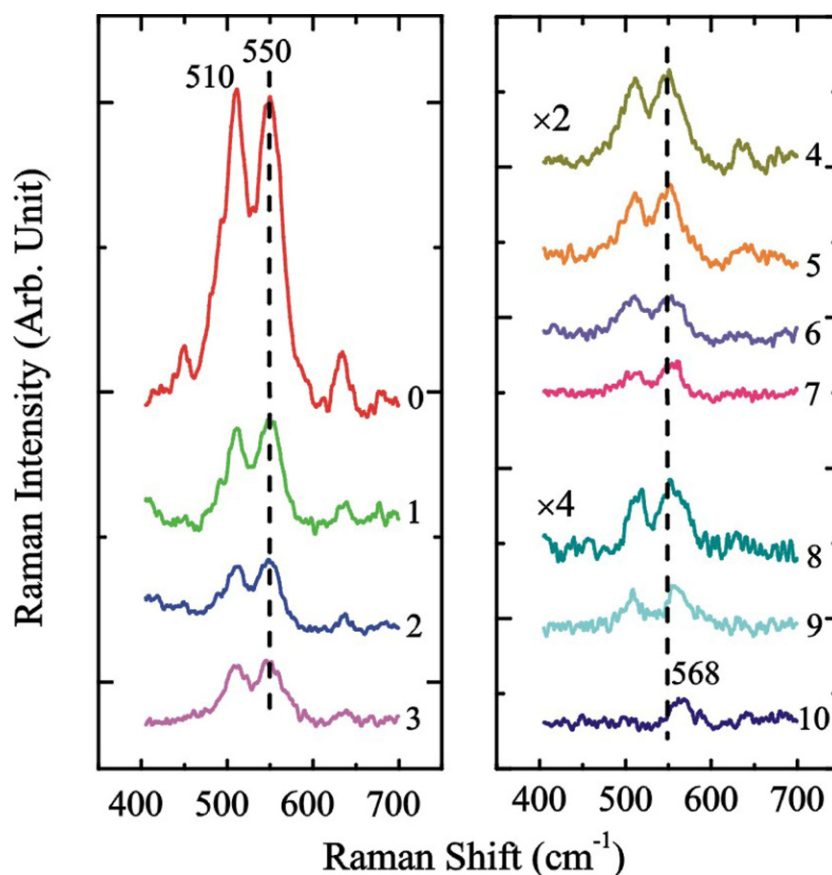
Figure 10. Raman spectra of the radial breathing modes of the lithium-doped 0.4 nm SWNTs excited using the 632.8 nm laser line. Spectrum 0 is for the pristine sample without lithium doping. Spectra 1–10 show Raman scattering of the samples with increasing density of lithium doping. The dashed line denotes the RBM of the pristine (5, 0) tube, which shifts from 550 to 568 cm^{-1} at saturated lithium doping.

the diameter. The lower frequency, G$^-$, is associated with carbon atom oscillation in the circumferential direction, which strongly depends on the tube diameter [48]. In tubes with diameter in the range of 0.9–3.0 nm, the separation between G^+ and G$^-$ can be fitted well with an empirical equation: $\omega_G^+ - \omega_G^- = C/d_t^2$, where the constant C is 47.7 cm^{-1} m^2 for semiconducting SWNTs and 79.5 cm^{-1} m^2 for metallic ones [50]. In very small SWNTs, the G$^-$ band can be shifted to a relatively low frequency. For example, $G^- = 1370$ cm^{-1} for the (4, 2) semiconducting tube, which has been clearly identified [39]. Spectrum 0 in figure 11 shows the Raman spectrum in the G$^+$ mode frequency region of the pristine sample. Four components, centred at 1558, 1586, 1599, and 1615 cm^{-1}, are identified. The three high-frequency components near the graphite-like G mode are attributed to the G$^+$ modes of the three co-existing tubes. The contributions from different tubes overlap and are indistinguishable. The component at 1558 cm^{-1} is relatively broad and weak, which can be attributed to E$_{1g}$ or E$_{2g}$ modes from the three tubes.

    In figure 11, we fitted the line shapes of different doping levels by three Lorentzians for three high-frequency peaks and one Breit–Wigner–Fano (BWF) line shape for the peak near
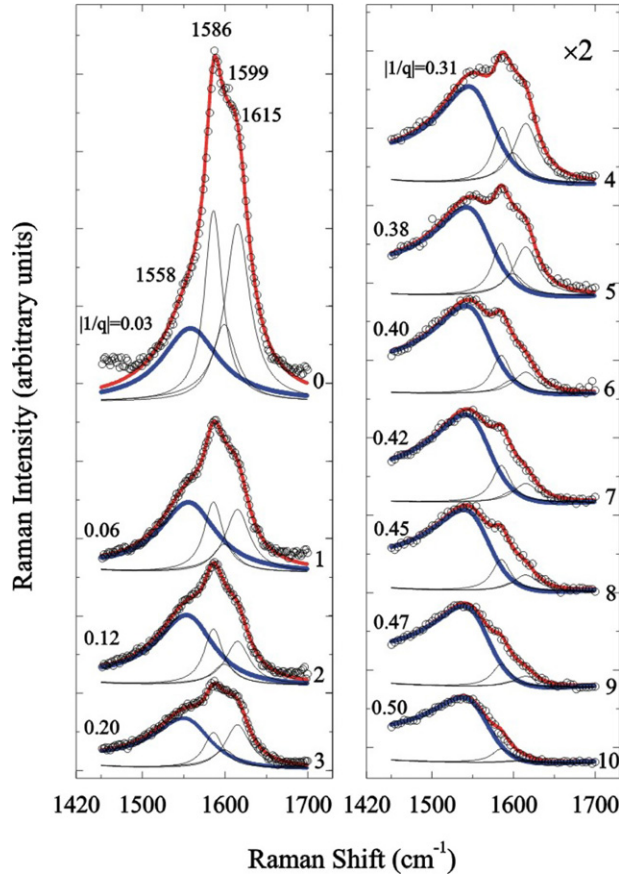
Figure 11. Raman spectra in the G$^+$ band frequency region excited using the 632.8 nm laser line. Spectrum 0 is the spectrum for the pristine sample without lithium doping. Spectra 1–10 show Raman scattering of the samples with from a low-level doping to saturated doping. The Raman bands are fitted using three Lorentzian (solid black curves) and one BWF (solid red curve) lineshapes. The coupling constant $(-1/q)$ is labelled on the left shoulder of each curve.

1558 cm^{-1}. The BWF line shape is given by

$$I(\omega) = I_0 \frac{[1 + (\omega - \omega_{\mathrm{BWF}})/q\Gamma]^2}{1 + [(\omega - \omega_{\mathrm{BWF}})/q\Gamma]^2},$$

where I_0, ω_{BWF}, and Γ are the intensity, renormalized frequency, and broadening parameter, respectively [51]. The asymmetric line shape is governed by $-1/q$, which characterizes the interaction between the discrete phonon states and the electronic continuum states [51]. We traced the line shapes of these G$^+$ bands as a function of the doping level. The behaviour of Lorentzians can be described mainly by intensity competition with a fixed line-width and centre frequency. In the BWF component near 1558 cm^{-1}, the variation is characterized by gradual changes of the line shape and a downshift in the peak frequency. In comparison with three high-frequency Lorentzians, the intensity of the BWF component decreases at a much slower pace and survives even at the highest doping level (spectrum 10). The Raman mode at 1558 cm^{-1} turns out to be the discrete phonon state coupled with the electronic continuum, which indicates the charge transfer from the lithium atom to the SWNTs. The $-1/q$ value of

the BWF component increases from 0.03 to 0.50 and the BWF frequency downshifts from 1558 to 1537 cm^{-1} with significant broadening in lineshape.

The value of $-1/q$ is proportional to the electron density at the Fermi level [51]. The $-1/q$ value obtained from the fitting for the SWNT@AFI sample is larger than the reported value for alkali-metal-doped SWNT bundles [43], but a factor of $\sim$2 smaller than that observed in the first-stage alkali metal graphite-intercalated compounds (MC$_8$, where M is K, Cs, and Rb). Qualitatively, a larger $-1/q$ value indicates a higher lithium doping concentration.

The peak frequency of the BWF lineshape in figure 11 is remarkably close to that observed in nanotubes with diameters of 1–2 nm [43]. The Raman spectrum at 1550 cm^{-1} indicates a general BWF region where coupling occurs between a discrete phonon mode and an electronic continuum. In large-diameter tubes, due to the small separation between the G$^+$ and G^- modes, the G^- band locates near the general BWF region and couples with the electronic continuum [51]. In our ultra-small SWNTs, the G$^-$ band is far away from the BWF region. Instead, the split G$^+$ modes appear there. It is the G^+ mode that couples with the electronic continuum to form the BWF line. The continuum spectra of the plasmon and the discrete phonon line couple to form the BWF line by a general Fano effect.

In summary, we have reviewed our recent study of Raman scattering on ultra-small SWNTs@AFI crystals. The Raman scattering technique is a convenient and powerful tool in characterization of structural and novel electronic properties of carbon nanotubes. The pyrolysis process of carbon precursors and the formation process of carbon nanotubes in the AFI zeolite channels were closely monitored using the Raman scattering technique, which greatly helped us to improve the nanotube sample quality. Thermal expansion behaviour and thermal stability of the 0.4 nm SWNTs, either confined in the AFI channels, or in the freestanding state, were systematically studied at different temperatures. The electronic states of the 0.4 nm SWNTs were modulated by means of lithium doping. The continuous electron charge transfer was *in situ* traced using Raman scattering.

Acknowledgments

References

[1] Iijima S and Ichibashi T 1993 *Nature* **363** 603
[2] Bethune D S, Kiang C H, de Vries M S, Gorman G, Savoy R, Vazquez J and Beyens R 1993 *Nature* **363** 605
[3] Sawada S and Hamada N 1992 *Solid State Commun.* **83** 917
[4] Cabria I, Mintmire J W and White C T 2003 *Int. J. Quantum Chem.* **91** 51
[5] Sun L F, Xie S S, Liu W, Zhou W Y, Liu Z Q, Tang D S, Wang G and Qiang L X 2000 *Nature* **403** 384
[6] Qin L C, Zhao X L, Hirahara K, Miyamoto Y, Ando Y and Iijima S 2000 *Nature* **408** 50
[7] Tang Z K, Sun H D, Wang J, Chen J and Li G 1998 *Appl. Phys. Lett.* **73** 2287
[8] Wang N, Tang Z K, Li G D and Chen J S 2000 *Nature* **408** 50
[9] Tang Z K, Wang N, Zhang X X, Wang J N, Chan C T and Sheng P 2003 *New J. Phys.* **5** 146.1–29
[10] Blase X, Benedict L X, Shirley E L and Louie S G 1994 *Phys. Rev. Lett.* **72** 1878
[11] Dresselhaus M S, Dresselhaus G and Eklund P C 1996 *Science of Fullerenes and Carbon Nanotubes* (San Diego, CA: Academic)
[12] Saito R, Dresselhaus G and Dresselhaus M S 1998 *Physical Properties of Carbon Nanotubes* (London: Imperial College Press)
[13] Li Z M *et al* 2001 *Phys. Rev. Lett.* **87** 127401
[14] Hulman M, Kuzmany H, Dubay O, Kresse G, Li L and Tang Z K 2003 *J. Chem. Phys.* **119** 3384

[15] Hulman M, Pfeiffer R and Kuzmany H 2004 *New J. Phys.* **6** 1
[16] Li Irene L, Li G D, Liu H J, Chan C T and Tang Z K 2003 *Appl. Phys. Lett.* **82** 1467
[17] Benedict L X, Crespi V H, Louie S G and Cohen M L 1995 *Phys. Rev.* B **52** 14935
[18] Tang Z K, Zhang L, Wang N, Zhang X X, Wen G H, Li G D, Wang J N, Chan C T and Sheng P 2001 *Science* **292** 2462
[19] Jiang F Y, Zhai J P, Ye J T, Han J R, Sheng P and Tang Z K 2005 *J. Cryst. Growth* **283** 108
[20] Chan Y F, Peng H Y, Tang Z K and Wang N 2003 *Chem. Phys. Lett.* **369** 541
[21] Wang N, Li G D and Tang Z K 2001 *Chem. Phys. Lett.* **339** 47
[22] Launois P, Moret R, Le Bolloc'h D, Albouy P A, Tang Z K, Li G and Chen J 2000 *Solid State Commun.* **116** 99
[23] Zhai J P, Tang Z K, Lam Frank L Y and Hu X J 2006 *J. Phys. Chem.* B **110** 19285
[24] Zhai J P, Li Z M, Liu H J, Li I L, Sheng P, Hu X J and Tang Z K 2006 *Carbon* **44** 1151
[25] Ye J T and Tang Z K 2005 *Phys. Rev.* B **72** 045414
[26] Li Z M, Zhai J P, Liu H J, Li I L, Chan C T, Sheng P and Tang Z K 2004 *Appl. Phys. Lett.* **85** 1253
[27] Guo J D *et al* 2004 *Phys. Rev. Lett.* **93** 017402
[28] Dresselhaus M S, Dresselhaus G, Charlier J C and Hernandez E 2004 *Phil. Trans. R. Soc.* A **362** 2065
[29] Dresselhaus M S, Dresselhaus G and Jorio A 2004 *Ann. Rev. Mater. Res.* **34** 247
[30] Raravikar N R, Keblinski P, Rao A M, Dresselhaus M S, Schadler L S and Ajayan P M 2002 *Phys. Rev.* B **66** 2354241
[31] Park S H, Kunstleve R W G, Graetsch H and Gies H 1997 *Progress in Zeolite and Microporous Materials, Pts a-C* vol 105 (Amsterdam: Elsevier Science B V) pp 1989–94
[32] Ci L J *et al* 2003 *Appl. Phys. Lett.* **82** 3098
[33] Lucas A A, Lambin P H and Smalley R E 1993 *J. Phys. Chem. Solids* **54** 587
[34] Tersoff J 1988 *Phys. Rev. Lett.* **61** 2879
[35] Liu H J and Chan C T 2002 *Phys. Rev.* B **66** 115416
[36] Robertson D H, Brenner D W and Mintmire J W 1992 *Phys. Rev.* B **45** 12592
[37] Li H D, Yue K T, Zhan Z L, Zhou L X, Zhang S L, Shi Z J, Gu Z N, Liu B B, Yang R S and Yang H B 2000 *Appl. Phys. Lett.* **76** 2053
[38] Huang F M, Yue K T, Tan P H, Zhang S L, Shi Z J, Zhou X H and Gu Z N 1998 *J. Appl. Phys.* A **84** 4022
[39] Jorio A *et al* 2002 *Chem. Phys. Lett.* **351** 27
[40] Ye J T, Li Z M, Tang Z K and Saito R 2003 *Phys. Rev.* B **67** 113404
[41] Metenier K, Bonnamy S, Beguin F, Journet C, Bernier P, Chapelle M L de La, Chauvet O and Lefrant S 2002 *Carbon* **40** 1765
[42] Peng L M, Zhang Z L, Xue Z Q, Wu Q D, Gu Z N and Pettifor D G 2000 *Phys. Rev. Lett.* **85** 3249
[43] Rao A M, Eklund P C, Bandow S, Thess A and Smalley R E 1997 *Nature* **388** 257
[44] Lee R S, Kim H J, Fischer J E, Thess A and Smalley R E 1997 *Nature* **388** 255
[45] Shimoda H, Gao B, Tang X P, Kleinhammes A, Fleming L, Wu Y and Zhou O 2002 *Phys. Rev. Lett.* **88** 015502
[46] Liu H J and Chan C T 2003 *Solid State Commun.* **125** 77
[47] Jorio A, Dresselhaus G, Dresselhaus M S, Souza M, Dantas M S S, Pimenta M A, Rao A M, Saito R, Liu C and Cheng H M 2000 *Phys. Rev. Lett.* **85** 2617
[48] Dresselhaus M, Dresselhaus G, Jorio A, Filho A S and Saito R 2002 *Carbon* **40** 2043
[49] Duesberg G S, Loa I, Burghard M, Syassen K and Roth S 2000 *Phys. Rev. Lett.* **85** 5436
[50] Jorio A, Filho A G S, Dresselhaus G, Dresselhaus M S, Swan A K, Goldberg B B, Pimenta M A, Hafner J H, Lieber C M and Saito R 2002 *Phys. Rev.* B **65** 155412
[51] Brown S D M, Jorio A, Corio P, Dresselhaus M S, Dresselhaus G, Saito R and Kneipp K 2001 *Phys. Rev.* B **63** 155414